



1 **A globally distributed dataset of coseismic**  
2 **landslide mapping via multi-source high-resolution**  
3 **remote sensing images**

4 Chengyong Fang<sup>1</sup>, Xuanmei Fan<sup>1\*</sup>, Xin Wang<sup>1</sup>, Lorenzo Nava<sup>2</sup>, Hao Zhong<sup>1,3</sup>, Xiujun Dong<sup>1</sup>,  
5 Jixiao Qi<sup>1</sup>, Filippo Catani<sup>2</sup>

6 <sup>1</sup>State Key Laboratory of Geohazard Prevention and Geoenvironment Protection, Chengdu  
7 University of Technology, 610059, Chengdu, China

8 <sup>2</sup>Machine Intelligence and Slope Stability Laboratory, Department of Geosciences, University  
9 of Padua, 35129 Padua, Italy

10 <sup>3</sup>College of Information Science and Technology, Chengdu University of Technology, 610059,  
11 Chengdu, China

12 *Correspondence to:* Xuanmei Fan ([fxm\\_cdut@qq.com](mailto:fxm_cdut@qq.com))

13

14



## 15 Abstract

16 Rapid and accurate landslide mapping following extreme triggering events is critical for  
17 emergency response, hazard prevention, and disaster management. Artificial intelligence-  
18 based approaches enable rapid landslide mapping, yet the lack of a high-resolution globally  
19 distributed and event-based dataset poses a severe challenge in developing generalized  
20 machine learning models for landslide detection. This paper addresses this issue by designing  
21 a diverse coseismic landslide dataset, the Globally Distributed Coseismic Landslide Dataset  
22 (GDCLD), which includes multi-source remote sensing images (i.e., PlanetScope, Gaofen-6,  
23 Map World, and Unmanned Aerial Vehicle) encompassing various geographical and geological  
24 backgrounds worldwide. The GDCLD can be accessed through this link:  
25 <https://doi.org/10.5281/zenodo.11369484> (Fang et al., 2024). Furthermore, we evaluate the  
26 potential of GDCLD by analyzing mapping performance of the seven most popular semantic  
27 segmentation algorithms. We further validate the generalization capabilities of the dataset by  
28 deploying the models on three types of remote sensing images from four independent regions.  
29 Besides, we also assess the model on rainfall-induced landslide dataset and achieve good  
30 results, demonstrating its applicability in landslide segmentation under other triggering factors.  
31 The results indicate the superiority of the proposed dataset in landslide detection, offering a  
32 robust mapping solution for rapid assessment in future extreme events that trigger landslides  
33 across the globe.

34

35



## 36 1. Introduction

37       Landslides triggered by extreme events such as earthquakes and heavy precipitation are  
38 responsible for most of the damage to mountainous settlements (Huang and Fan, 2013). In  
39 some cases, landslides can be even more disastrous than the triggering events themselves, as  
40 they can render emergency responses ineffective by cutting off roads and other transportation  
41 lifelines (Cigna et al., 2012; Huang et al., 2012; Valagussa et al., 2019; Chau et al., 2004).  
42 Therefore, the rapid and accurate identification of landslides after extreme events is crucial for  
43 timely and quantitative assessment of disasters. This is especially important for emergency  
44 rescue operations and subsequent risk management in mountainous areas with complex  
45 environments and possibly inconvenient transportation routes. (Cigna et al., 2018; Chau et al.,  
46 2004; Gorum et al., 2011).

47       Conventional landslide mapping efforts rely on traditional surveying methods such as  
48 topographic total stations, field observations to collect essential data on slope stability and  
49 terrain morphology (Brardinoni et al., 2003; Coe et al., 2003; Zhong et al., 2020). These  
50 methods may not capture the full extent of terrain dynamics due to their static nature  
51 (Metternicht et al., 2005). Consequently, these methods are not effective for detailed landslide  
52 mapping, especially when traversing the affected and unstable regions for field surveys is not  
53 possible. This was particularly true for the Wenchuan co-seismic landslides, which mobilized  
54 large amounts of material that obstructed roads, complicating disaster response efforts as well  
55 as surveying and mapping activities (Gorum et al., 2011). With the development of remote  
56 sensing technology in the past decades, landslide investigation has been supported by digital  
57 mapping, which reduces time and labor costs (Fiorucci et al., 2011; Fiorucci et al., 2019; Gao  
58 and Maro, 2010; Guzzetti et al., 2012). This mapping has also been enhanced by various  
59 modalities of sensors, such as synthetic aperture radar (Mondini et al., 2021; Nava et al., 2021),  
60 multi-spectral (Udin et al., 2019), and hyper-spectral (Ye et al., 2019). However, visual  
61 identification is highly subjective due to operator experience, and the interpretation of events  
62 involving numerous landslides is still time-consuming. Therefore, this subjectivity and the time-



63 consuming nature of interpretation hinder the reliability and efficiency of landslide mapping,  
64 especially after major events such as the Wenchuan, China (2008), and Gorkha, Nepal (2015)  
65 earthquakes.

66 Generally, the ideal solution is to develop automated models or tools that can save time  
67 and costs while ensuring an objective protocol in the mapping process (Casagli et al., 2023).  
68 While some researchers have endeavored to employ machine learning or deep learning in  
69 constructing these models, most of them lack the generalization capability for application across  
70 diverse environmental backgrounds and remote sensing images (Burrows et al., 2019; Bhuyan  
71 et al., 2023; Li et al., 2016; Liu et al., 2022; Lu et al., 2019; Luppino et al., 2022; Meena et al.,  
72 2021; Soares et al., 2022; Yang et al., 2022a). To improve such models, more abundant data  
73 that consider the diverse geomorphological and climatic settings where landslides occur are  
74 essential. The Bijie landslide dataset, based on Map World image, presents a small-scale  
75 dataset of mountainous landslides, filling the gap in landslide detection tasks for the first time  
76 (Ji et al., 2020). Landslide4sense, based on Sentinel-2 image, introduces a multispectral  
77 landslide dataset, pioneering semantic-level annotation of landslides (Ghorbanzadeh et al.,  
78 2022). The HRGLDD and GVLM datasets, based on PlanetScope and Google Earth image  
79 respectively, propose global-scale high-resolution landslide datasets (Meena et al., 2022;  
80 Zhang et al., 2023). However, these datasets are limited by their reliance on single remote  
81 sensing data sources, restricting the applicability of models across different sensors and  
82 resolutions. The CAS dataset introduces a mountain landslide dataset containing various  
83 remote sensing data sources (Xu et al., 2024). However, due to its limited annotated landslide  
84 quantity, high image overlap, and lack of negative samples (background/non-landslide), it is still  
85 insufficient to effectively generalize to landslide automatic mapping tasks in various complex  
86 environments especially where signatures of landslides often resemble nearby terrain.

87 Therefore, there is a pressing need for the development of a carefully curated and diverse  
88 dataset. Such a dataset would facilitate the rapid and accurate mapping of landslides using  
89 available prior knowledge. Hence, we present a comprehensive landslide dataset derived from  
90 nine earthquake-triggered landslide occurrences, encompassing multi-sensor images from 3m-



91 PlanetScope, 2m-Gaofen-6, 0.5m-Map World, and 0.2m-UAV. This work addresses the  
92 shortcomings of existing datasets in terms of accuracy and generalization for training large and  
93 complex deep-learning models. It is of great significance for accurate, rapid, and automatic  
94 mapping of landslide events occurring anywhere in the world, providing strong support for  
95 efficient geohazard emergency response and investigation.

## 96 2. Relate work

97 The current effective method for landslide mapping involves image segmentation, and  
98 computer vision segmentation tasks heavily rely on effective data to build segmentation models.  
99 Compared to other computer tasks, landslide segmentation tasks have emerged relatively late,  
100 with only a small number of studies constructing datasets for different landslide events. In this  
101 section, we review some landslide segmentation datasets and introduce their specific  
102 information.

103 The Bijie landslide dataset comprises high-resolution satellite images captured in  
104 landslide-prone areas of Guizhou province, China. The dataset includes 770 landslide samples  
105 and 2,003 non-landslide samples. The positive samples consist of rockfalls, rockslides, and a  
106 small number of debris avalanches, while the negative samples include mountains, villages,  
107 roads, rivers, and farmland, among others. The image resolutions vary from 61×61 pixels to  
108 1,239×1,197 pixels, with RGB channels. There is a total of  $7.23 \times 10^6$  pixels assigned for  
109 landslide within the dataset (Ji et al., 2020).

110 The landslide4sense dataset consists of multispectral satellite images captured across four  
111 distinct regions. This dataset comprises 3,799 images, each with dimensions of 64×64 pixels  
112 and a spatial resolution of 10 meters. Each image contains 14 bands, including 12 bands from  
113 the Sentinel-2 satellite and 2 bands from Digital Elevation Model (DEM) data. The dataset  
114 includes negative background samples such as bare soil, rivers, and buildings. There is a total  
115 of  $1.76 \times 10^6$  pixels assigned for landslide within the dataset (Ghorbanzadeh et al., 2022).

116 The HR-GLDD spans 10 distinct geographic regions, capturing landslide instances across  
117 various geographical environments in South Asia, Southeast Asia, East Asia, South America,



118 and Central America. HR-GLDD comprises a total of 1,756 image patches, each standardized  
119 to a size of 128×128 pixels with a spatial resolution of up to 3 meters. The dataset is sourced  
120 from four spectral bands of the PlanetScope satellite. It includes a variety of negative samples,  
121 such as non-landslide terrain features, buildings, and roads, ensuring a comprehensive  
122 representation for model training. There is a total of  $2.96 \times 10^6$  pixels assigned for landslide  
123 within the dataset (Meena et al., 2022).

124 The GVLM dataset spans across six continents and 17 different landslide sites, GVLM  
125 covers a diverse range of geological and climatic conditions, from the lush landscapes of Asia  
126 to the rugged terrain of South America. Comprising 17 pairs of dual-temporal VHR images,  
127 each image pair boasts a spatial resolution of 0.59 meters, ensuring detailed capture of  
128 landslide features and their surrounding environments. GVLM incorporates various negative  
129 samples, including non-landslide landforms, infrastructure such as buildings, and transportation  
130 networks, providing a holistic training ground for models. Image sizes within the GVLM dataset  
131 range from 1,861×1,749 pixels to 10,828×7,424 pixels. There is a total of  $3.24 \times 10^7$  pixels  
132 assigned for landslide within the dataset (Zhang et al., 2023).

133 The CAS Landslide Dataset covers nine different geographic regions spanning South Asia,  
134 Southeast Asia, East Asia, South America, and Central America. Comprising 20,865 image  
135 patches, each standardized to a size of 512×512 pixels, the dataset offers a spatial resolution  
136 ranging from 0.2 to 5 meters. During the cropping process, an overlap setting parameter of 0.5  
137 was used. These images are sourced from unmanned aerial vehicles (UAVs) and satellite  
138 platforms, integrating data from the PlanetScope satellite and other sources. The dataset  
139 removes background images that do not contain landslide pixels and therefore lacks sufficient  
140 background noise as negative samples to enhance the robustness of the model. There is a total  
141 of  $1.95 \times 10^8$  pixels assigned for landslide within the dataset (Xu et al., 2024).

142 In summary, comparing with other remote sensing detection tasks such as land cover/use,  
143 the currently available landslide datasets are exceedingly scarce, predominantly comprising  
144 single remote sensing images with low spatial resolutions. Overall, the available landslide  
145 datasets are exceedingly limited, primarily comprising single remote sensing images with low



146 spatial resolution. Most crucially, these datasets lack sufficient annotations of landslide  
147 instances, exhibit high overlap, and suffer from a dearth of diverse negative samples. As a  
148 result, they are ill-equipped to tackle the challenges of mapping landslides in large-scale areas  
149 with complex background objects, especially those sharing spectral and textural characteristics  
150 with landslide surfaces, such as bare soil and rocks. Furthermore, they fail to provide adequate  
151 data sources for effectively training large-scale neural network baseline models.

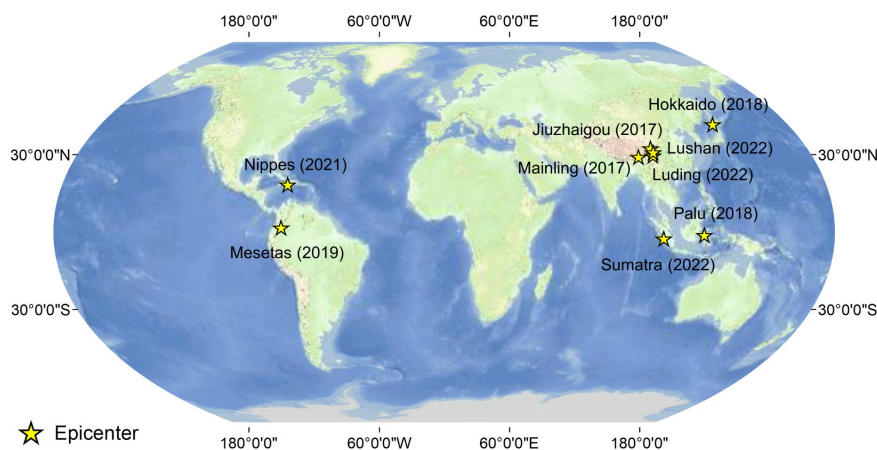
152 **Table.1** Existing landslide dataset statistics

Dataset	Bands	Tiles	Size	Labeling pixels
Bijie landslide	3	2,773	61×61 ~ 1,197~1,239	7.23×10 <sup>6</sup>
Landslide4sense	14	3,799	64×64	1.76×10 <sup>6</sup>
HR-GLDD	4	1,756	128×128	2.96×10 <sup>6</sup>
GVLN	3	17	1,861×1,749 ~ 10,828×7,424	3.24×10 <sup>7</sup>
CAS Landslide	3	20,865	512×512	1.95×10 <sup>8</sup>

### 153 3. Globally Distributed Coseismic Landslide Dataset 154 (GDCLD)

#### 155 3.1 Data collection

156 Our dataset encompasses a catalog of landslides triggered by nine seismic occurrences,  
157 delineated across the Himalayan seismic belt and the Circum-Pacific belt, as depicted in  
158 Figure.1. These regions have witnessed actively seismic events with magnitudes over 5.9,  
159 triggering numerous landslides. We obtained data of these locations from various remote  
160 sensing sources. This section delineates the particulars of the seismic events and the  
161 provenance of the remote sensing data.



162

★ Epicenter

163

**Figure.1** Location distribution of earthquake-induced landslide events

164

### 3.1.1 The 2017 Jiuzhaigou earthquake-triggered landslides

165

166

167

168

169

170

171

172

173

174

175

176

177

### 3.1.2 The 2017 Mainling earthquake-triggered landslides

178

179

180

181

182

On November 18, 2017, a magnitude 6.4 earthquake struck Mainling County (95.02°E, 29.75°N), resulting in three injuries and affecting 12,000 individuals. The earthquake triggered over 1,000 landslides, obstructing numerous watercourses and covering a total area of 33.61km<sup>2</sup>, with the largest landslide spanning 4.9km<sup>2</sup> (Hu et al., 2019). Mainling County, located on the southeastern margin of the Qinghai-Tibet Plateau within the Yarlung Zangbo Grand





183 Canyon, is part of the Mediterranean Himalayan seismic zone. This region, with altitudes  
184 ranging from 800 to 7,782m and an average elevation of 2,500m, features a maximum elevation  
185 differential of 2,000m and a robust vegetation coverage of 60% (Gao et al., 2023; Chen et al.,  
186 2019). The monsoonal climate here brings annual rainfall between 1,500 and 2,000mm (Huang  
187 et al., 2021). Following the earthquake, we acquired 3m-resolution PlanetScope images on  
188 December 17, 2017, and April 08, 2018, to interpret the landslides (Figure.S2).

### 189 **3.1.3 The 2018 Hokkaido earthquake**

190 On September 6, 2018, a Mw 6.6 earthquake struck Hokkaido, Japan (142.01°E, 42.69°N),  
191 resulting in 44 fatalities and over 660 injuries. Approximately 80% of the casualties were due to  
192 coseismic landslides. The earthquake triggered over 7,800 landslides, causing extensive  
193 damage to infrastructure. The total area affected by landslides was 23.77 km<sup>2</sup>, with the largest  
194 individual landslide covering 0.5km<sup>2</sup> (Wang et al., 2019). The region, which receives an annual  
195 precipitation of 1,200–1,800mm—relatively low compared to other parts of Japan (Yamagishi  
196 and Yamazaki, 2018)—is characterized by sandstone, mudstone, siltstone, and shale  
197 formations, overlain by substantial volcanic sediments (Wang et al., 2019). Following the  
198 Jiuzhaigou earthquake, we acquired PlanetScope image with a 3m resolution on December 12,  
199 2018, and Map World image with a 0.5m resolution (Figure.S3).

### 200 **3.1.4 The 2018 Palu earthquake**

201 On September 28, 2018, the Palu region of Sulawesi, Indonesia, was struck by a Mw 7.5  
202 earthquake with a focal depth of 10 km (0.18°S, 119.84°E). A detailed analysis by Shao et al.  
203 (2023) identified approximately 15,700 co-seismic landslides across a 14,600km<sup>2</sup> area, with a  
204 combined landslide area of about 43.0km<sup>2</sup>. These landslides were predominantly concentrated  
205 in the mountainous canyon regions south of the epicenter. This study provides a semantic-level  
206 interpretation of these landslides, which were mainly shallow disruptions (Shao et al., 2023).  
207 However, some larger-scale flow slides, rockfalls, and debris flows were also observed. High-  
208 resolution Map World image (1m) was utilized to support this analysis (Figure.S4).

209 earthquake

### 210 **3.1.5 The 2019 Mesetas earthquake**



211 The research site is located in the eastern foothills of the Colombian Eastern Cordillera.  
212 On December 24, 2019, the Mesetas Earthquake, with a magnitude of 6.0, struck this region,  
213 as documented by Poveda et al. (2022). The earthquake's epicenter was located at 76.19°W,  
214 3.45°N, triggering approximately 800 co-seismic landslides. The distribution and predominant  
215 orientation of these landslides were influenced by the shear zone confined within the Guapecito  
216 Fault, a subsidiary offshoot of the Algeciras Fault (Poveda et al., 2022). High-resolution  
217 PlanetScope images (3m) was acquired on January 5 and February 12, 2020, to analyze these  
218 phenomena (Figure.S5).

### 219 **3.1.6 The 2021 Nippes earthquake**

220 On August 14, 2021, a Mw 7.2 earthquake struck the Nippes Mountains in Haiti (73.45°W,  
221 18.35°N). This seismic event, compounded by heavy rainfall from Tropical Storm Grace on  
222 August 16-17, triggered numerous secondary geological hazards across the Tiburon Peninsula.  
223 The disaster resulted in at least 2,246 fatalities and injured over 12,763 individuals (Calais et  
224 al., 2022). The earthquake-induced landslides totaled 4,893, covering an estimated 45.6km<sup>2</sup>,  
225 with the largest individual landslide spanning 3.1×10<sup>5</sup> m<sup>2</sup> (Zhao et al., 2022b). The affected area,  
226 with elevations up to 2,300 m (Alpert, 1942), consists mainly of volcanic rocks, such as basalts,  
227 and sedimentary formations, particularly limestones (Harp et al., 2016). Post-earthquake, we  
228 utilized 3m-resolution PlanetScope image (August 29, 2022) and 0.5m-resolution Map World  
229 image to assess the damage (Supplementary Figure 6).

230 On August 14, 2021, a seismic event registering Mw 7.2 hit in the Nippes Mountains of  
231 Haiti (73.45°W, 18.35°N). This seismic activity, coupled with substantial rainfall from Tropical  
232 Storm Grace between August 16 and 17, precipitated a significant number of secondary  
233 geological hazards in the Tiburon Peninsula. The calamity resulted in a tragic loss of at least  
234 2,246 lives and inflicted injuries upon more than 12,763 individuals (Calais et al., 2022). The  
235 earthquake triggered a total of 4,893 landslides, covering an estimated area of 45.6km<sup>2</sup>, with  
236 the maximum individual area reaching 3.1×10<sup>5</sup>m<sup>2</sup> (Zhao et al., 2022b). The study area,  
237 characterized by elevations reaching up to 2,300 m above sea level (Alpert, 1942). Comprised  
238 predominantly of volcanic rocks, such as basalts, and sedimentary formations, notably



239 limestones (Harp et al., 2016). In addition to obtaining 3m-resolution PlanetScope image after  
240 the Nippes earthquake, we also acquired 0.5m-resolution Map World image (Figure.S6).

### 241 **3.1.7 The 2022 Sumatra earthquake**

242 On February 25, 2022, a Mw 6.1 earthquake struck West Sumatra, Indonesia, at a shallow  
243 depth of 4.9 km. The epicenter was located approximately 20 km from Mount Talakmau  
244 (100.10°E, 0.22°N), a compound volcano rising to about 3,000m. Mount Talakmau, active  
245 during the Holocene, consists of andesite and basalt from the Pleistocene-Holocene epoch  
246 (Basofi et al., 2016). The earthquake induced extensive landslides over a 6km<sup>2</sup> area on the  
247 volcano's eastern and northeastern flanks. High-resolution PlanetScope image (3m) from  
248 March 5 and April 24, 2022, captured these landslides (Figure.S7).

### 249 **3.1.8 The 2022 Lushan earthquake**

250 On June 1, 2022, an Mw 5.9 earthquake (102.94°E, 30.37°N) struck Lushan County, China,  
251 resulting in 4 fatalities and 42 injuries, affecting 14,427 individuals. The seismic event triggered  
252 1,063 landslides over a total area of 7.2km<sup>2</sup>, with the largest landslide covering 0.3km<sup>2</sup> (Zhao  
253 et al., 2022a). This region, located on the southeast margin of the Qinghai-Tibet Plateau,  
254 features an average elevation exceeding 2,000m, with altitudes ranging from 557 to 4,115m  
255 (Tang et al., 2023). It is characterized by lush vegetation covering 80% of the area and  
256 experiences a subtropical monsoon climate with annual rainfall between 1,100 and 1,300mm  
257 (Chen et al., 2019). The geological composition predominantly consists of exposed sandstones  
258 and mudstones (Zhao et al., 2022a). High-resolution imagery, including 3 m-resolution  
259 PlanetScope images, 0.5m-resolution Map World image, and 0.2m-resolution UAV images  
260 acquired on June 13, 2022, using a Sony ILCE-5100, was collected for the affected region  
261 (Figure.S8).

### 262 **3.1.9 The 2022 Luding earthquake**

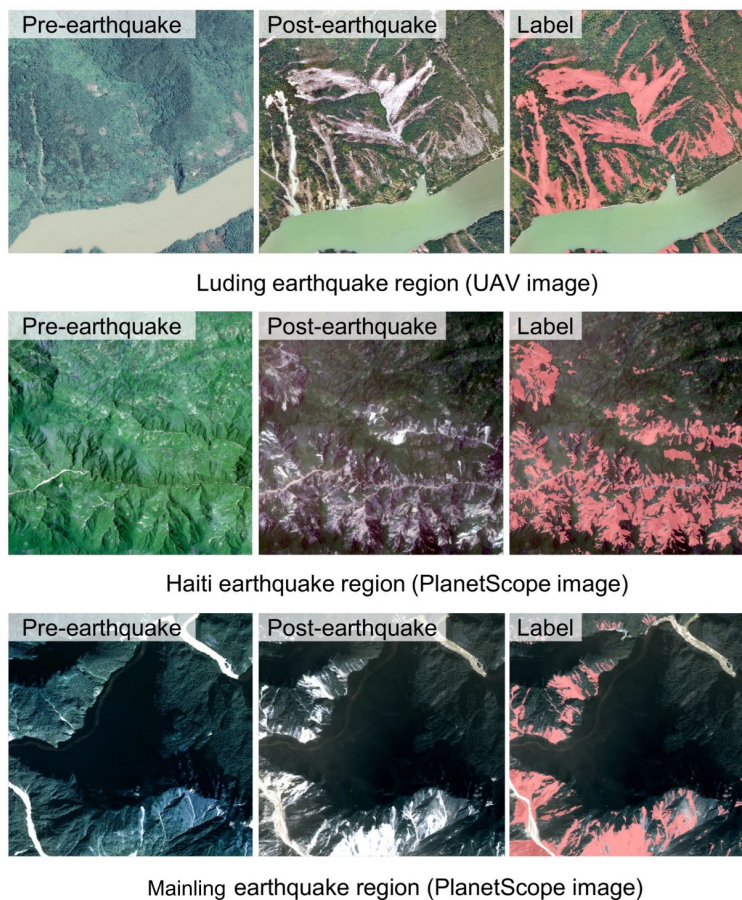
263 On September 5, 2022, an Mw 6.8 earthquake struck Luding County, China (102.08°E,  
264 29.59°N), resulting in 93 fatalities. The seismic event triggered approximately 15,000 landslides  
265 over an area of 28.53km<sup>2</sup>, with the largest individual landslide covering 2.4×10<sup>6</sup>m<sup>2</sup> (Dai et al.,  
266 2023). This region lies on the southeastern margin of the Qinghai-Tibet Plateau within the "Y"-



267 shaped Xianshuihe Fault Zone (Yang et al., 2022b). The geological composition predominantly  
268 includes limestone, sandstone, dolomite, and some intrusive rocks (Dai et al., 2023). In the  
269 aftermath of the earthquake, rapid rescue operations and data collection were undertaken,  
270 utilizing 0.2m-resolution UAV image (acquired on October 7, 2022, via Phase One IXU1000),  
271 3m-PlanetScope image (acquired on September 25, 2022), Map World image (0.5m), and  
272 Gaofen-6 (2m) (Figure.S9).

### 273 3.2 Preprocessing of landslide dataset

274 In the aforementioned nine events, given the focus of public data on geological analysis  
275 rather than semantic segmentation tasks. After performing multi-source data spatial registration,  
276 atmospheric correction and radiometric calibration on remote sensing images, we used QGIS  
277 for landslide interpretation. These labels were delineated with reference to pre-earthquake  
278 remote sensing imagery and post-earthquake multi-source remote sensing image. By  
279 comparing spectral disparities and analyzing morphological attributes between bi-temporal  
280 images, we mapped the semantic landslide labels. (Figure.2).

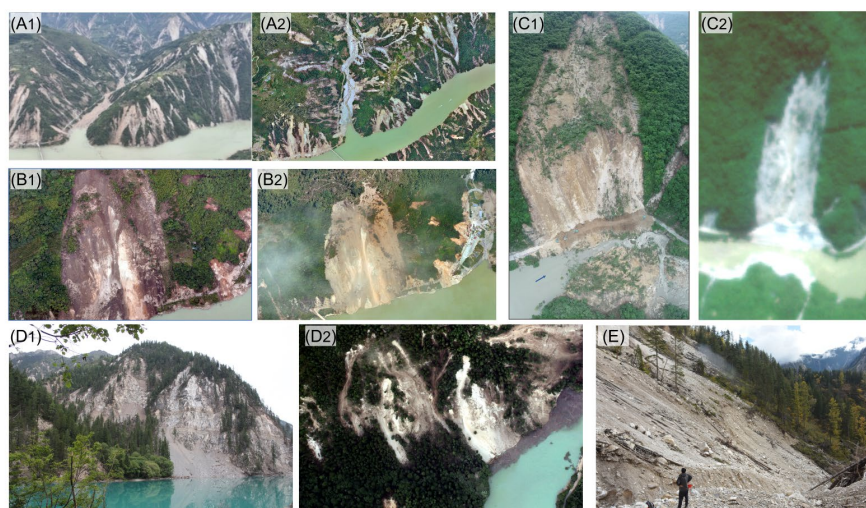


281  
282 **Figure.2** Remote sensing images before and after the earthquake and landslide interpretation  
283 results (landslides marked in red).

284 Moreover, we actively participated in emergency response and field investigation after  
285 these major earthquakes in China. This further improved the reliability of the landslide  
286 inventories. Figure.3 showcases photographs captured on-site after the Jiuzhaigou earthquake,  
287 Lushan earthquake, and Luding earthquake. Specifically, Figures 3 (A<sub>1</sub>) and 3 (B<sub>1</sub>) were taken  
288 in Luding, Sichuan, depicting the extensive devastation caused by concentrated coseismic  
289 landslides, impacting Wandonghe Village and resulting in severe destruction of local  
290 infrastructure. Corresponding aerial photos with a resolution of 0.2m, Figures 3 (A<sub>2</sub>) and 3 (B<sub>2</sub>),  
291 offer a comprehensive perspective of the affected area. Figure 3 (C<sub>1</sub>), taken in Lushan, Sichuan,



292 captures the consequences of the earthquake-triggered large landslide dam, which obstructed  
293 the river channel. The corresponding PlanetScope image, Figure 3 (C<sub>2</sub>), provides an overhead  
294 view of the altered landscape. Furthermore, Figure 3 (D<sub>1</sub>), taken in the Jiuzhaigou Panda Sea,  
295 illustrates a significant volume of landslide deposits reaching the sea, with the accompanying  
296 UAV image at a resolution of 0.2m, Figure 3 (D<sub>2</sub>), offering detailed insights. Lastly, Figure 3 (E)  
297 presents a field work photo involved in these surveys. These field investigations serve to  
298 enhance comprehension and subsequent calibration on our remote sensing interpretation.



299  
300 **Figure.3** Comparison of field survey photos and remote sensing images: A<sub>1</sub> and A<sub>2</sub> are the  
301 Wandong landslides induced by the 2022 Luding earthquake; B<sub>1</sub> and B<sub>2</sub> are the Dadu River  
302 Bridge landslide induced by the 2022 Luding earthquake; C<sub>1</sub> and C<sub>2</sub> are the Baoxing landslides  
303 induce by the 2022 Lushan earthquake; D<sub>1</sub> and D<sub>2</sub> are the Panda sea landslides induced by  
304 the 2017 Jiuzhaigou earthquake; E is a photo of field work at Jiuzhaigou.

305 To obtain semantic-level annotations for landslide labels, all remote sensing images were  
306 converted into RGB images (8-bit). the preprocessing stage was conducted through three steps:  
307 binary mask generation, data sampling, and image patching. First, utilizing the Rasterio library  
308 in Python, landslide vector labels for each selected region were transformed into binary masks,  
309 where 1 denoted landslide and 0 represented background. Subsequently, regions densely  
310 populated with landslides were sampled, and both remote sensing images and masks were



311 patched and cropped into regular grids, yielding patches of 1,024×1,024 pixels. To mitigate  
 312 interference among patches, overlap parameter was set as 0. Given the obvious imbalance  
 313 between non-landslide and landslide areas, we manually removed most of the images without  
 314 any landslide pixel annotations. The ratios of positive landslide samples and negative non-  
 315 landslide samples were 8.01% and 91.99%, respectively. Table.2 presents detailed information  
 316 regarding different remote sensing data sources for each study case.

317 **Table.2** Detailed information of each event in GDCLD

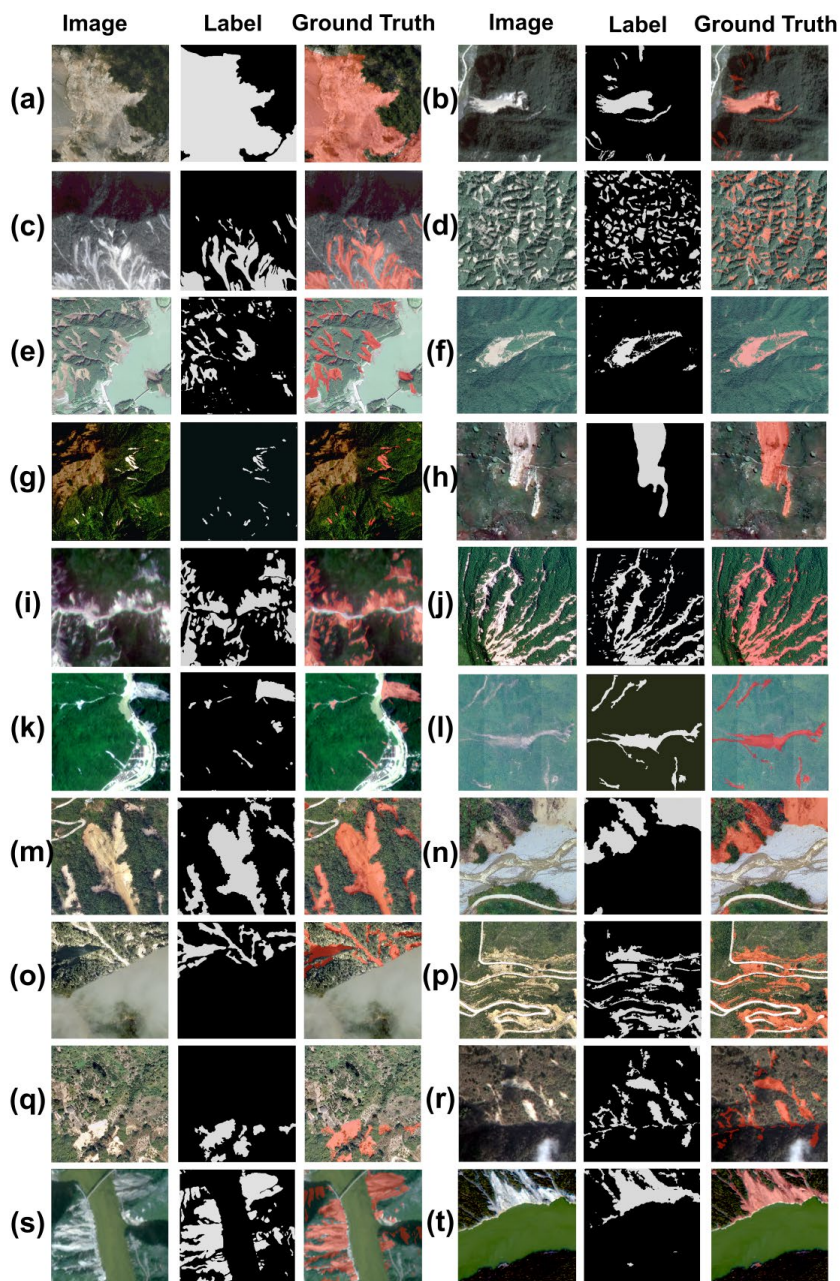
Events	Data sources	Resolution	Number of tiles
Jiuzhaigou 2017 (Mw 6.5)	UAV	0.2m	2,288
	PlanetScope	3m	176
Mainling 2017 (Mw 6.4)	PlanetScope	3m	118
Hokkaido 2018 (Mw 6.6)	Map World	0.5m	796
	PlanetScope	3m	123
Palu 2018 (Mw 7.5)	Map World	1m	335
Mesetas 2019 (Mw 6.0)	PlanetScope	3m	144
Haiti 2021 (Mw 7.2)	PlanetScope	3m	238
	Map World	0.5m	404
Sumatra 2022 (Mw 6.1)	PlanetScope	3m	110
	UAV	0.2m	210
	Map World	0.5m	182
Lushan 2022 (Mw 5.9)	PlanetScope	3m	110
	UAV	0.2m	9,252
	Map World	0.5m	1,540
Luding 2022 (Mw 6.6)	GF-6	2m	496



	PlanetScope	3m	190
Sum	-	-	16712

318 Additionally, to enhance the robustness and generalization capability of deep learning  
319 models, a subset of background noise elements such as clouds, roads, buildings, bare land,  
320 and rocks were manually selected as negative non-landslide samples. The negative samples  
321 can be outlined as follows: diverse roads (Figure.4: (e), (k), (m), (n), (p), (s)), river channels  
322 (Figure.4: (e), (k), (n), (s), (t)), clouds (Figure.4: (o), (r)), barren land (Figure. 4: (c), (h), (q)).  
323 Additionally, human-engineered structures and buildings are also considered (Figure.4: (e), (k)).





324

325 **Figure.4** Display of landslide sample data from different study areas and different remote  
326 sensing data sources: Jiuzhaigou UAV (a), Jiuzhaigou PlanetScope (b), Mainling PlanetScope  
327 (c), Hokkaido PlanetScope(d), Hokkaido Map World (e), Palu Map World (f), Mesetas



328 PlanetScope (g), Haiti Map World (h), Haiti PlanetScope (i), Sumatra PlanetScope (j), Lushan  
329 PlanetScope (k), Lushan UAV (l), Luding UAV(m~q), Luding Map World (r), Luding PlanetScope  
330 (s), and Luding Gaofen-6 (t).

## 331 4. Experimental setup

332 After the completion of dataset construction, the experimental phase follows. In this section,  
333 we will introduce several semantic segmentation algorithms used for validating the dataset, the  
334 loss functions and accuracy evaluation metrics employed in the experiments, as well as various  
335 hyperparameter settings utilized during the experiments.

### 336 4.1 Segmentation algorithms

337 In this section, we have selected seven of the most popular semantic segmentation  
338 networks, including four models based on the CNN architecture and three based on the  
339 Transformer architecture. These seven algorithms have medium to large-scale parameter sizes  
340 and computational complexities, and show excellent performance in a variety of remote sensing  
341 semantic scenarios, making them suitable for precision comparison and validation of novel  
342 datasets.

343 (1) UNet: As one of the earliest and most renowned semantic segmentation models, UNet  
344 is distinguished by its unique U-shaped architecture (Ronneberger et al., 2015). This design  
345 facilitates efficient learning and precise localization by combining high-resolution features from  
346 the contracting path with up-sampled outputs from the expanding path. Both the encoder and  
347 decoder in UNet are composed purely of CNN structures (O'shea and Nash, 2015). This  
348 simplicity, along with a relatively small number of parameters, allows UNet to achieve  
349 exceptional accuracy and rapid inference on small datasets. Consequently, it is widely utilized  
350 in applications such as small-scale object classification, change detection, and medical imaging.

351 (2) ResUNet: ResUNet is an advanced variant of the UNet model, incorporating residual  
352 connections to enhance its performance and learning efficiency (Diakogiannis et al., 2020). The  
353 key innovation in ResUNet is the integration of residual blocks within both the encoder and



354 decoder paths, which address the vanishing gradient problem and enable the training of deeper  
355 networks (He et al., 2016). These residual blocks allow the network to learn identity mappings,  
356 facilitating gradient flow through the network and improving convergence rates. Similar to UNet,  
357 ResUNet maintains a U-shaped architecture that combines high-resolution features from the  
358 contracting path with up-sampled outputs from the expanding path, ensuring precise  
359 localization and context capture. The combination of residual connections improves feature  
360 reuse and learning efficiency, enabling ResUNet to effectively improve Recall and small target  
361 detection capabilities in semantic segmentation tasks.

362 (3) DeepLabV3: DeepLabV3, is a semantic segmentation model known for its  
363 sophisticated use of atrous convolution, or dilated convolution (Chen et al. 2018). This  
364 technique allows the network to capture multi-scale contextual information without losing spatial  
365 resolution, addressing the limitations of traditional convolutional networks in dense prediction  
366 tasks. DeepLabV3 incorporates atrous spatial pyramid pooling to robustly segment objects at  
367 multiple scales by applying atrous convolution with different rates in parallel. This model also  
368 integrates features from both the encoder and decoder paths, enhancing the precision of  
369 boundary delineation. In addition, the architecture of DeepLabV3 utilizes batch normalization  
370 and depth-separable convolution. This design can effectively reduce the complexity and  
371 computational cost of the model, while enabling the model to have stronger feature extraction  
372 capabilities and generalization than simple networks such as UNet.

373 (4) HRNet: High-Resolution Network (HRNet) is noted for its innovative approach to  
374 maintaining high-resolution representations throughout the network (Wang et al., 2020). Unlike  
375 traditional models that gradually down-sample the input to extract features, HRNet preserves  
376 high-resolution features by maintaining parallel high-to-low resolution subnetworks. This design  
377 allows HRNet to integrate multi-scale information effectively, ensuring precise localization and  
378 robust feature representation. The network continuously exchanges information across  
379 different resolutions, resulting in superior accuracy and detailed segmentation results. Due to  
380 its ability to retain fine-grained spatial information and adapt to various scales, HRNet excels in  
381 complex tasks such as fine-grained terrain classification, semantic segmentation in urban



382 scenes, and fine-grained visual detection.

383 (5) UperNet: UperNet employs a pyramid feature extraction method, integrating multi-scale  
384 information to capture contextual details across different resolutions (Xiao et al., 2018; Liu et  
385 al., 2022). It utilizes a Feature Pyramid Network (FPN) backbone for hierarchical feature  
386 extraction, enhanced by a global context integration module to enrich overall scene  
387 understanding. Additionally, UperNet incorporates lateral connections for efficient  
388 communication between feature pyramid levels, ensuring seamless information flow and  
389 accurate segmentation. This sophisticated architecture enables UperNet to achieve superior  
390 segmentation performance, particularly in challenging scenarios with complex scenes and  
391 diverse object scales.

392 (6) SwinUNet: Built upon the Swin Transformer architecture, SwinUNet blends self-  
393 attention mechanisms with UNet for exceptional performance (Cao et al., 2022). It inherits Swin  
394 Transformer's hierarchical feature extraction for capturing both local and global contextual  
395 information efficiently (Liu et al., 2021). The self-attention mechanism enables capturing  
396 nuanced relationships in data. SwinUNet integrates UNet's contracting and expanding paths in  
397 decoding, emphasizing spatial detail preservation. This combination empowers SwinUNet to  
398 excel in tasks requiring precise localization and robust contextual understanding. (7)

399 SegFormer: SegFormer, represents a significant advancement in semantic segmentation by  
400 leveraging a transformer-based architecture (Xie et al., 2021). Unlike traditional CNN  
401 approaches, SegFormer employs a hierarchical transformer encoder to capture multi-scale  
402 contextual information effectively, without relying on complex designs such as positional  
403 encodings or large pre-training datasets. The decoder in SegFormer integrates features from  
404 different scales using lightweight multi-layer perceptron, ensuring efficient and precise  
405 segmentation. This innovative design enables SegFormer to achieve excellent segmentation  
406 results with medium-sized parameters and fast inference speed in high-resolution complex  
407 scenes.4.2 Model training



## 408 4.2 Loss function and accuracy evaluation

409 Since the landslide detection is a two-class semantic segmentation task, we choose the  
410 Binary Cross-Entropy (De Boer et al., 2005) as the loss function for model training, whose  
411 mathematical expression is shown as follow:

$$412 \quad L(y, \hat{y}) = -\frac{1}{N} \sum_{i=1}^N [y_i \log(\hat{y}_i) + (1-y_i) \log(1-\hat{y}_i)] \quad (1)$$

413 where  $L$  is the loss function,  $N$  is the number of samples,  $y_i$  is the true label (0 or 1) of the  $i$ -th  
414 sample, and  $\hat{y}_i$  is the predicted probability of the  $i$ -th sample.

415 For accuracy evaluation, the following accuracy indicators are calculated through  
416 confusion matrices (Townsend, 1971): precision, recall, F1 score (Chicco and Jurman, 2020)  
417 and mean intersection over union (mIoU) (Rezatofighi et al., 2019). Their calculation formulas  
418 are as follows:

$$419 \quad \text{Precision} = \frac{TP}{TP+FP} \quad (2)$$

$$420 \quad \text{Recall} = \frac{TP}{TP+FN} \quad (3)$$

$$421 \quad F1 = \frac{2 \times \text{Precision} \times \text{Recall}}{\text{Precision} + \text{Recall}} \quad (4)$$

$$422 \quad \text{mIoU} = \frac{1}{N} \sum_{i=1}^N \frac{TP_i}{TP_i + FP_i + FN_i} \quad (5)$$

423 where the TP is the True Positive, FP is the False Positive, TN is the True Negative and FN is  
424 the False Negative.

## 425 4.3 Equipment and Parameter

426 The deep learning framework employed in this study is conducted based on PaddlePaddle  
427 2.3.2 (Ma et al., 2019), with the environment configured for Python 3.8, CUDA 11.2, and CuDNN  
428 8.3.0. The experimental setup encompasses Intel Xeon CPU, W2255, 3.7GHz, equipped with  
429 256GB of system memory. The GPU infrastructure consists of Tesla V100, with 32GB of video  
430 memory. The operating system employed is Ubuntu 20.04. The model's optimizer is selected  
431 as AdamW (Loshchilov and Hutter, 2017), with an initial learning rate of 0.0006, beta1 set to  
432 0.9, beta2 to 0.999, weight decay to 0.01 and epoch to 100.



## 433 5. Results

434 To validate the accuracy of the GDCLD dataset, this study will select four types of remote  
435 sensing images (UAV, PlanetScope, Map World image, and Gaofen-6) from five seismic events  
436 (Luding, Jiuzhaigou, Hokkaido, Mainling, and Nippes) as training and validation datasets for  
437 model construction and accuracy evaluation. The ratio of training dataset to validation dataset  
438 is 3:1. Subsequently, to assess the excellent generalization ability of this landslide dataset, we  
439 will choose three types of remote sensing images (UAV, PlanetScope, and Map World image)  
440 from the independent four seismic events (Lushan, Mestas, Sumatra, and Palu) as the test  
441 dataset for generalization testing.

442 We conducted evaluations on our dataset utilizing the aforementioned seven semantic  
443 segmentation algorithms. After each model is trained for 100 epochs, we meticulously  
444 examined the performance of the GDCLD dataset in landslide identification. we present the  
445 performance of the seven algorithms on the validation dataset in Table.3.

446 Among these seven algorithms, UNet, ResUNet, DeeplabV3, and HRNet serve as neural  
447 network models with convolutional structures, whereas UperNet, SwinUNet, and SegFormer  
448 are based on transformer-based neural network architectures. From Table.3, it is evident that  
449 Transformer-based semantic segmentation models exhibit superior performance compared to  
450 models based on convolutional structures. Overall, the mIoU of the seven algorithms on  
451 GDCLD validation set spans from 71.07% to 85.06%. Notably, UNet demonstrates the least  
452 detection with the mIoU and F1 score of 71.07% and 79.54%. In contrast, SegFormer yields  
453 the best performance with the accuracy of 91.35%, recall of 91.70%, F1 score of 91.52%, and  
454 mIoU of 85.06%. Figure.5 illustrates the detection results of different models across various  
455 remote sensing data sources. it can be seen that transformer-based semantic segmentation  
456 models achieve superior segmentation outcomes.

457

458

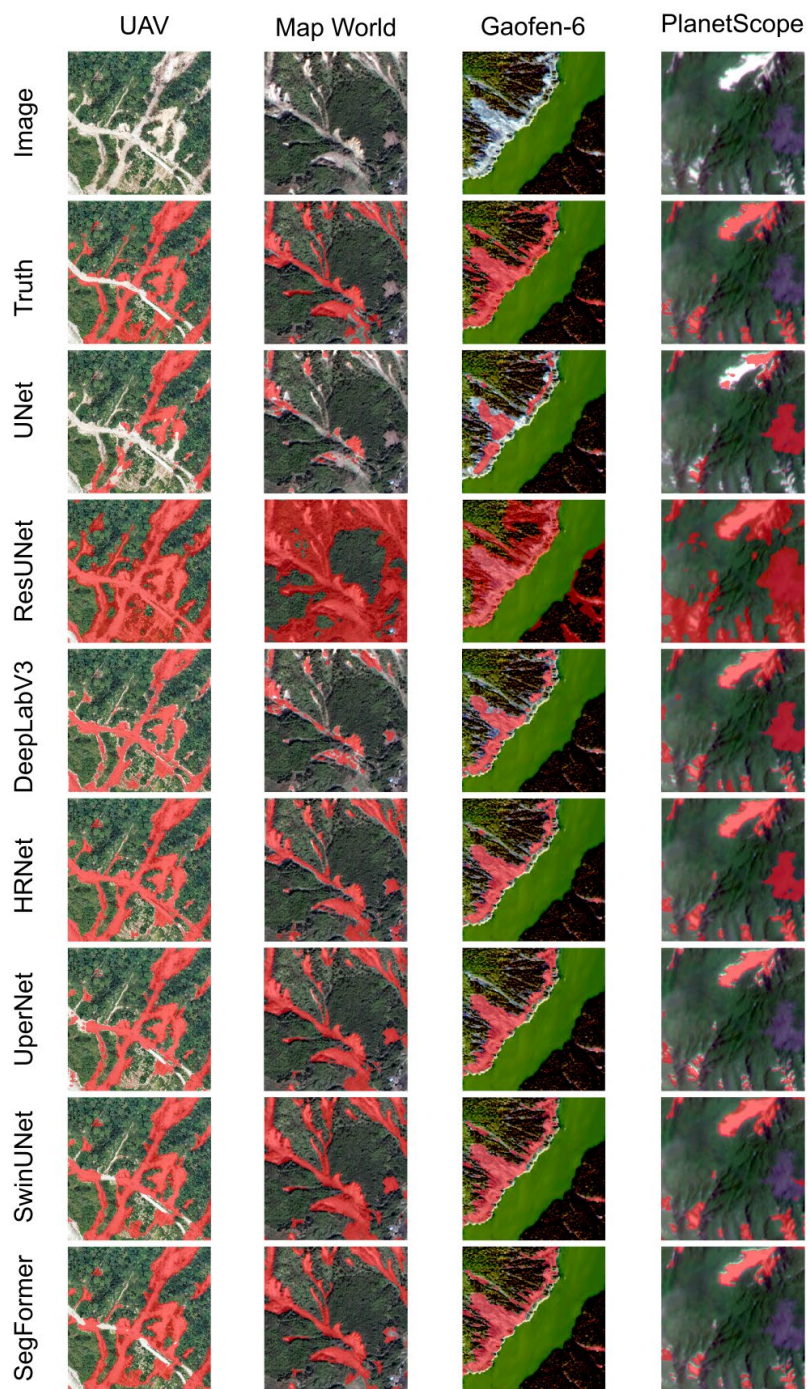
459



460

**Table.3** Comparison of result on GDCLD validation dataset

Method	Backbone	Precision (%)	Recall (%)	F1 (%)	mIoU (%)
UNet	-	77.05	82.01	79.54	71.07
ResUNet	ResNet-50	78.17	86.48	82.11	71.94
DeepLabV3	ResNet-50	81.27	86.96	84.02	74.61
HRNet	HRNet-48	81.88	87.21	84.46	75.19
UperNet	ViT-B16	88.18	90.64	89.39	81.97
SwinUNet	-	89.78	<b>92.01</b>	90.72	83.68
SegFormer	MiT-B4	<b>91.35</b>	91.70	<b>91.52</b>	<b>85.06</b>



461  
462

**Figure.5** Comparative results of different algorithms on validation dataset





463 To demonstrate the robustness and generalization capability of the dataset-trained models  
464 in other environment, we conducted testing by using four independent events, as illustrated in  
465 Table.4. Overall, the mIoU performance of the algorithms trained on GDCLD ranges from 56.09%  
466 to 72.84%. SegFormer exhibits the best performance, achieving precision of 77.09%, recall of  
467 87.09%, F1 score of 81.88%, and mIoU of 72.84%. we present detailed results of six types of  
468 remote sensing images in these four events in Table.5. The overall mIoU ranges from 69.01%  
469 to 82.31%, while the F1 ranges from 80.63% to 89.30%. Furthermore, we noticed a remarkable  
470 imbalance between Recall and Precision in the predicted results. The recall is always higher  
471 than the precision, as it is crucial to not miss any important landslides for disaster assessment  
472 and rescue operations. From the perspective of remote sensing sensors, except for the  
473 Sumatra incident, higher resolution was directly related to better landslide detection  
474 performance.

475 **Table.4** Comparison of result on test dataset

Method	Backbone	Precision (%)	Recall (%)	F1 (%)	mIoU (%)
UNet	-	61.69	61.22	61.45	56.09
ResUNet	ResNet-50	66.56	64.46	65.49	57.06
DeepLabV3	ResNet-50	65.26	67.75	66.48	59.73
HRNet	HRNet-48	65.52	72.03	68.62	61.79
UperNet	ViT-B16	69.96	78.08	73.80	65.42
SwinUNet	-	71.56	82.26	76.54	67.18
SegFormer	MiT-B4	<b>77.09</b>	<b>87.09</b>	<b>81.88</b>	<b>72.84</b>

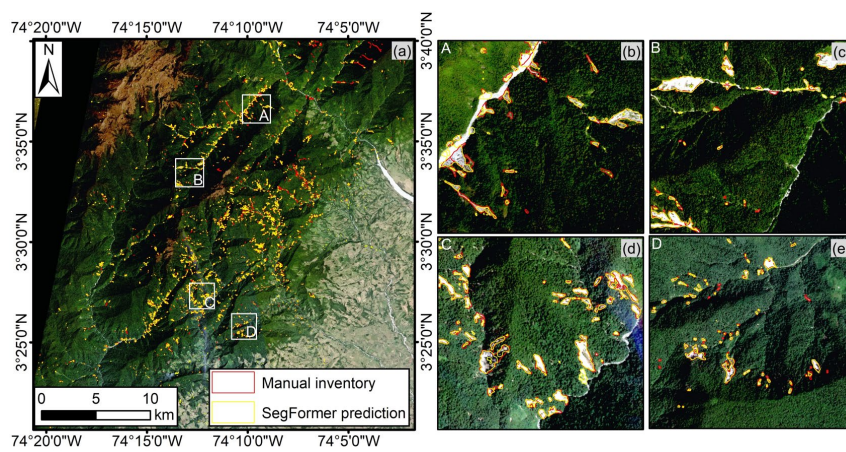
476 **Table.5** Detection results of SegFormer in different events

Events	Image type	Precision (%)	Recall (%)	F1 (%)	mIoU (%)
	UAV	74.72	90.35	81.80	72.96
Lushan	Map World	76.18	87.35	81.38	71.92
	PlanetScope	81.50	82.28	81.78	69.05
Palu	Map World	73.48	91.24	81.40	71.12
Mesetas	PlanetScope	80.26	80.97	80.63	69.01
Sumatra	PlanetScope	83.57	97.45	89.30	82.31

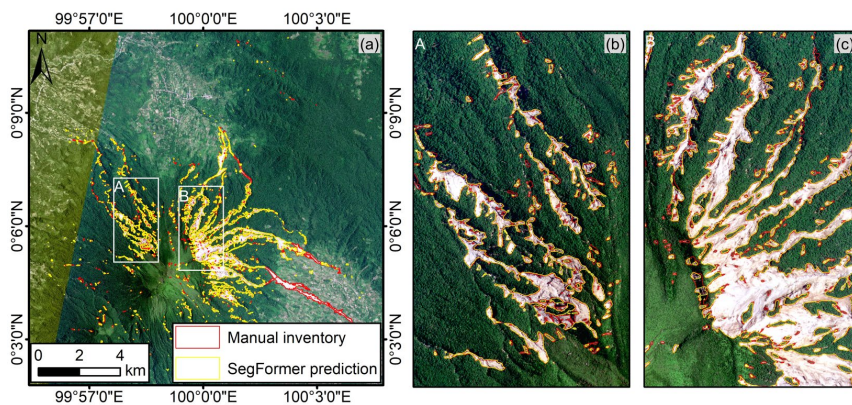
477 Figures.6 to 9 respectively illustrate the detection results for Mesetas (PlanetScope),



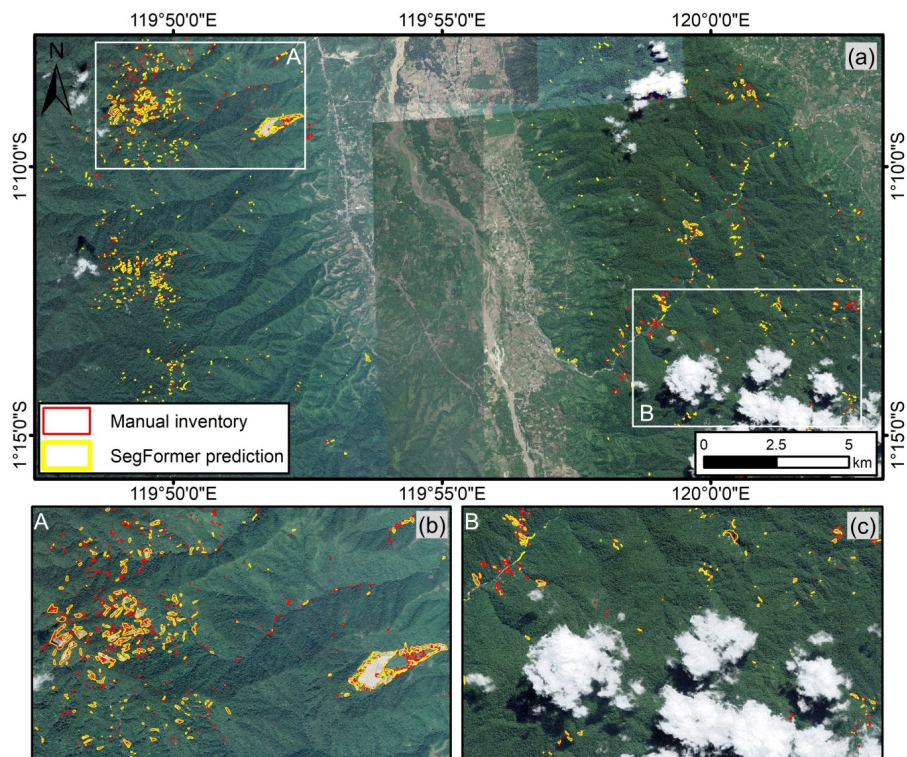
478 Sumatra (PlanetScope), Palu (Map World image), and Lushan (UAV). The F1 score of the  
479 Mesetas event model is 80.63%, with recall and precision exhibiting relative balance. As  
480 observed in Figure.6, our model demonstrates strong capabilities in detecting and segmenting  
481 the majority of landslides, particularly in regions of mountainous slopes (Figure.6 (d)). In areas  
482 affected by mountain shadows (Figure.6 (b, c, e)), as expected, since, pixel signatures of  
483 shadows are very different than those of landslides. The model effectively identifies most large  
484 landslides but exhibits some omissions in detecting small landslides. In the Sumatra event, we  
485 attained remarkably excellent detection results, with F1 score of 89.30%, Recall of 97.45%, and  
486 Precision of 83.57%, Recall is 13.88% higher than Precision. As illustrated in Figure.7, the  
487 model effectively identifies nearly all landslides (Figure.7 (b, c)). However, there are instances  
488 of missed landslide detection in the lower-right corner of Figure.7 (a). This is due to the apparent  
489 confusion between the landslide accumulation area and river channels, resulting in sub-optimal  
490 detection. In the Palu event, our F1 score yielded a result of 81.40%, with Recall reaching 91.24%  
491 and Precision by 73.48%, Recall is 17.76% higher than Precision. As depicted in Figure.8, the  
492 detection outcomes effectively discriminate between numerous cloud obscuration, bare lands,  
493 and buildings, underscoring the positive efficacy of augmenting negative samples in our dataset  
494 to improve the model's detection capabilities. Similarly, for the Lushan event captured by UAV,  
495 we achieved the F1 score of 81.80%, with Recall and Precision of 90.35% and 74.72%, Recall  
496 exceeding Precision by 15.63%. As shown in Figure.9, in the UAV data, the model  
497 demonstrates exceptional segmentation capabilities for large-scale landslides (Figure.9 (b, c,  
498 d)), while its detection performance for some small-scale disasters is less satisfactory. Overall,  
499 the model trained based on GDCLD demonstrated excellent generalization capabilities across  
500 four independent test datasets. It successfully detected all major landslides and effectively  
501 segmented landslide boundaries. More importantly, the model effectively excluded background  
502 noise from river channels, bare ground in residential areas, and cloud region, showcasing its  
503 remarkable robustness.



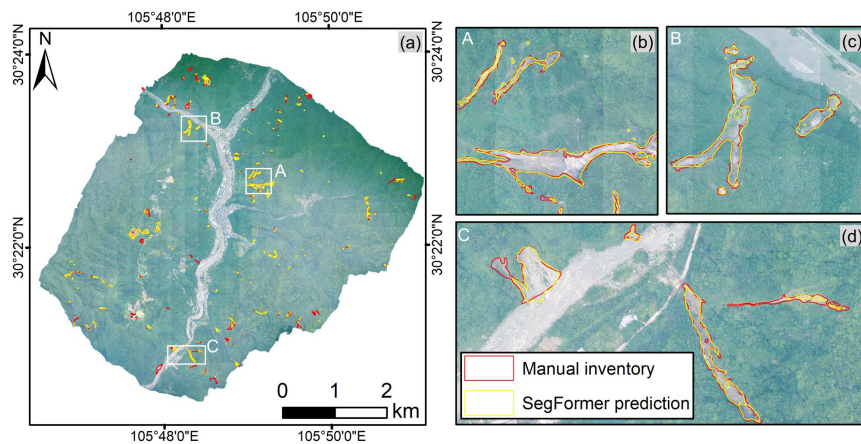
504  
505 **Figure.6** Mesetas PlanetScope dataset. (a) Regional aerial view. (b-e) Detection results of four  
506 magnified areas.



507  
508 **Figure.7** Sumatra PlanetScope dataset. (a) Regional aerial view. (b-c) Detection results of two  
509 magnified areas.



510  
511 **Figure.8** Palu Map World dataset. (a) Regional aerial view. (b-c) Detection results of two  
512 magnified areas.  
513



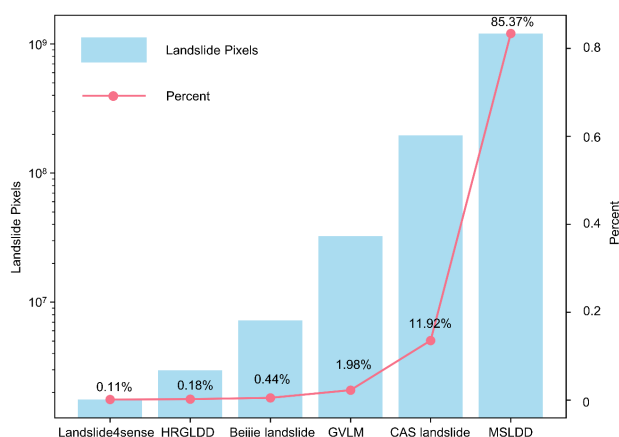
514  
515 **Figure.9** Lushan UAV dataset. (a) Regional aerial view. (b-d) Detection results of three  
516 magnified areas.



## 517 6. Discussion

### 518 6.1 Sample richness of GDCLD

519 The GDCLD dataset stands out as the most extensive and comprehensive repository of  
520 landslide data currently available, encompassing landslide data from various geographic  
521 environments and multiple remote sensing sources. the annotated landslide labels within this  
522 dataset tally up to approximately  $1.39 \times 10^9$  pixels, roughly six times as many annotations as all  
523 the other publicly accessible landslide datasets (Figure.10). Additionally, this dataset includes  
524 a variety of negative samples with optical characteristics similar to landslides which can  
525 significantly enhance the model's generalization capability. In contrast to other datasets, which  
526 are limited to training small-scale semantic segmentation models like UNet and DeepLabV3  
527 (Xu et al., 2024; Meena et al., 2022; Ghorbanzadeh et al., 2022), the GDCLD dataset can  
528 effectively train large-scale semantic segmentation models such as Transformers. Moreover,  
529 unlike Sentinel-2 and Landsat satellite image, where moderate spatial resolutions can limit the  
530 accurate delineation of landslide boundaries, GDCLD provides remarkably high spatial  
531 resolutions (0.2m~3m) and diverse spectral characteristics. This dataset not only performs well  
532 in landslide mapping across diverse geographical settings, but also serves as a baseline  
533 dataset for transfer learning in landslide detection.



534



535 **Figure.10** Statistical comparison of landslide pixels in different landslide datasets.

## 536 6.2 Enhancement in model generalization

537 In the GDCLD dataset, a general selection of remote sensing data from multiple sources  
538 enhances the overall generalization capability of the landslide identification model. To  
539 substantiate this assertion, we conduct a comparative analysis between models trained by  
540 single- and multi-source datasets. The datasets from different sensors are segregated, and the  
541 SegFormer, which is an advanced and widely used transformer-based algorithm, is applied to  
542 train the landslide models. Their performance was verified by their respective test dataset as  
543 well as an independent event of Lushan earthquake.

544 The accuracy metrics for the validation dataset are presented in Table.6. Across four  
545 remote sensing sources—PlanetScope, Gaofen-6, Map World, and UAV—models trained on  
546 single-source datasets consistently demonstrate higher performance on test samples, with  
547 mIoU indices surpassing those of multi-source datasets by 2.26%, 1.63%, 0.64%, and 0.13%,  
548 respectively. However, a noteworthy observation emerges when models are transferred to the  
549 independent Lushan earthquake case (Table.7). The model trained on the multi-source dataset  
550 achieves significantly enhanced performance compared to the model derived from single-  
551 source counterpart. The mIoU of UAV-, Map World- and PlanetScope based datasets are  
552 improved by 8.16%, 7.95% and 0.09%. As depicted in Figure.11, the models trained by multi-  
553 source images exhibit higher recalls, accurate landslide boundaries, and robust resistance to  
554 interference. The yellow circle highlights the enhancements of models trained by multi-source  
555 images compared to single-source images. From the perspective of data sources, Map World  
556 contains different types of images (such as Maxer and Worldview), encompassing multitude of  
557 spectral responses across these sensors. the UAV image in the Lushan event utilize the sensor  
558 different from those in the Luding and Jiuzhaigou event, resulting in noticeable spectrum  
559 differences in images. Consequently, compared to a single remote sensing source, the  
560 generalization capability of the models trained by multi-source images demonstrate a more  
561 pronounced improvement. In contrast, the PlanetScope image, obtaining from the same



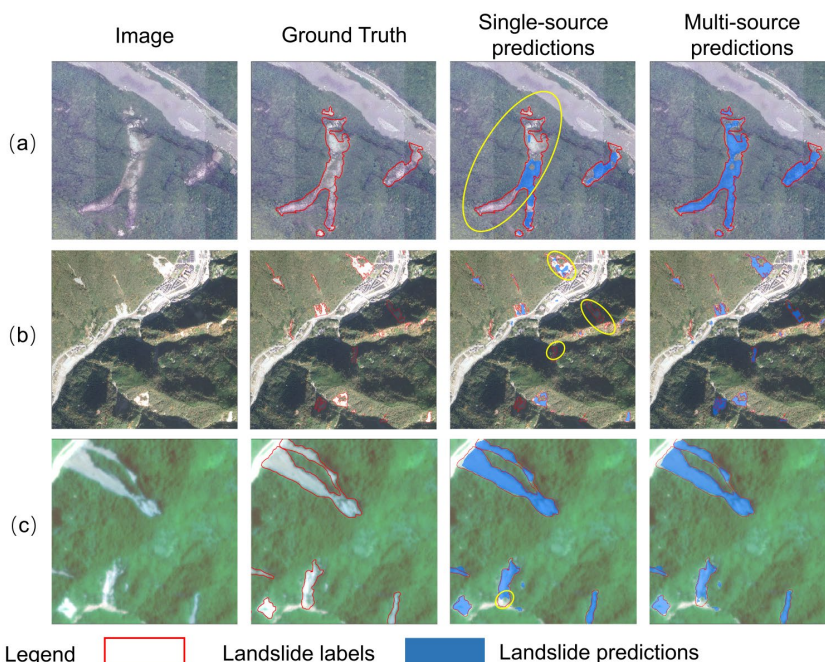
562 satellite sensors, exhibits smaller spectral variations in various images. As a result, the model  
 563 trained on both single and multi-source datasets achieve similar performance. This highlights  
 564 the importance of datasets with diverse images sources for enhanced model performance in  
 565 landslide mapping. This indicate that the utilization of multi-source remote sensing datasets  
 566 enables the model to learn the spectral characteristics of the images from diverse sensors.  
 567 Hence, the model trained by GDCLD possesses enhanced generalization ability and  
 568 robustness, enabling it to effectively perform landslide mapping in independent cases without  
 569 prior knowledge.

570 **Table.6** GDCLD performances on validation dataset through single- and multi-source dataset

Data source	Data type	Precision (%)	Recall (%)	F1 (%)	mIoU (%)
Single source	UAV	<b>92.20</b>	<b>92.90</b>	<b>92.54</b>	<b>87.07</b>
	PlanetScope	<b>87.98</b>	<b>87.81</b>	<b>87.89</b>	<b>80.11</b>
	Map World	<b>86.49</b>	<b>90.01</b>	<b>88.21</b>	<b>80.66</b>
	Gaofen-6	<b>91.25</b>	<b>88.04</b>	<b>89.62</b>	<b>83.61</b>
Multiple source	UAV	91.91	92.64	92.27	86.94
	PlanetScope	85.01	87.79	86.37	77.85
	Map World	86.42	89.12	87.74	80.02
	Gaofen-6	90.49	85.20	87.77	81.98

571 **Table.7** GDCLD performances on unseen dataset through single- and multi-source dataset

Data source	Data type	Precision (%)	Recall (%)	F1 (%)	mIoU (%)
Single source	UAV	64.92	<b>90.68</b>	75.67	64.80
	PlanetScope	81.25	<b>82.29</b>	81.75	68.96
	Map World	68.39	80.16	73.81	63.97
Multiple source	UAV	<b>74.72</b>	90.35	<b>81.80</b>	<b>72.96</b>
	PlanetScope	<b>81.50</b>	82.28	<b>81.78</b>	<b>69.05</b>
	Map World	<b>76.18</b>	<b>87.35</b>	<b>81.38</b>	<b>71.92</b>



572

573 **Figure.11** Comparative results of ablation experiments between multi- and single-source (a).

574 UAV, (b). Map World, (c). PlanetScope

### 575 6.3 Model based on GDCLD performance on existing datasets

576 To assess the robustness and generalization capabilities of the GDCLD dataset, we  
577 employ SegFormer trained on the GDCLD dataset (G-S model) to identify landslides within  
578 three distinct datasets: HR-GLDD, GVLM, and CAS. Initially, we standardize the data from  
579 these three datasets into 1024×1024 remote sensing tiles. Subsequently, utilizing the M-S  
580 model, we conduct landslide identification across all these datasets. Table.8 demonstrates  
581 favorable performance of the model across these diverse datasets. For instance, in the HR-  
582 GLDD dataset, which shares similarities with the PlanetScope image within GDCLD, the model  
583 achieves an mIoU of 76.97%, indicating a balance between Precision and Recall metrics.  
584 Similarly, when applied to the GVLM dataset, leveraging Map World image, our dataset exhibits  
585 robust predictive outcomes, resulting in a comprehensive mIoU of 70.07%. Likewise, for the  
586 CAS dataset, GDCLD demonstrates strong generalization capabilities, yielding an outstanding



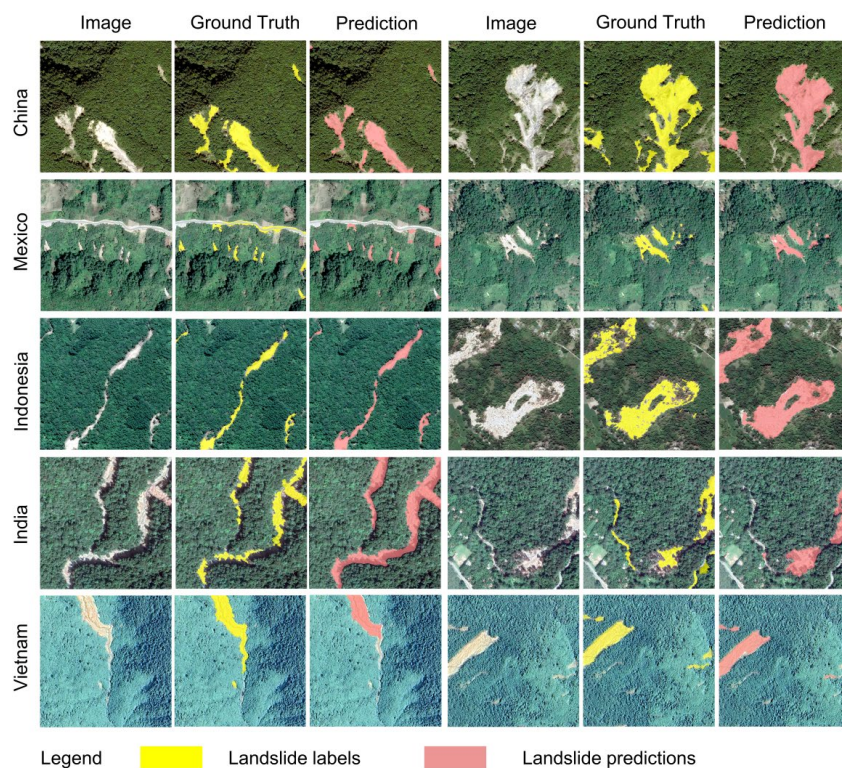


587 comprehensive metric with mIoU = 76.91%, alongside balanced Recall and Precision metrics.  
588 Although all landslide samples contained in GDCLD are induced by seismic activity, our  
589 model demonstrates good detection capabilities for rainfall-induced landslides. These two  
590 categories exhibit distinct spectral characteristics from their surrounding environments.  
591 Consequently, models trained on GDCLD exhibit proficient detection capabilities for rainfall-  
592 induced landslides (cite). We present the identification performance of GDCLD-based model  
593 for rainfall-induced landslides from the GVLM dataset in Table.8 and Figure.12. Figure.12  
594 underscores the excellent detection performance of the M-S model on rainfall-induced  
595 landslides in the GVLM dataset. Despite occasional misclassifications of small-size targets, the  
596 model effectively delineates the majority of rain-induced landslides. the precision metrics in  
597 Table.8 affirm this observation with an mIoU reaching 78.22% and both recall and precision  
598 exceeding 85%. This highlights the robust generalization capability of the model trained by our  
599 dataset, enabling effective identification of rainfall-induced landslides.

600

**Table.8** Validation results of other public datasets

Dataset	Precision (%)	Recall (%)	F1 (%)	mIoU (%)
HR-GLDD	84.88	86.81	85.84	76.97
GVLM	72.83	87.54	80.68	70.07
CAS	82.95	86.35	84.62	76.91
GVLM-rainfall	85.88	86.71	86.29	78.22



602 **Figure.12** Detection results of rainfall landslides by G-S model in GVLM dataset

## 603 7. Data availability

604 The data is freely available at <https://doi.org/10.5281/zenodo.11369484> (Fang et al., 2024).  
605 There are compressed folders, namely train\_dataset.zip, val\_dataset.zip and test\_dataset.zip.  
606 The train\_dataset.zip file contains 11,162 TIFF-format RGB images and their corresponding  
607 binary label data, with each image having dimensions of 1024×1024 pixels. The val\_dataset.zip  
608 file comprises 4,459 TIFF-format RGB images and binary label data, with each image also  
609 sized at 1024×1024 pixels. The test\_data.zip file includes seven original remote sensing  
610 images from four landslide events, with images in TIFF-format RGB and labels in TIFF-format  
611 binary data, though the image dimensions vary. For each label, "0" indicates the background,  
612 while "1" denotes the landslide. In addition, the other original data of UAV, Map World and  
613 Gaofen-6 are non-public data. If you need to use them, please contact the corresponding author.



614 The original PlanetScope imageries can be found at <https://www.planet.com/> (Planet Team,  
615 2019).

## 616 8. Code availability

617 Code used to produce data described in this paper, as well as to create figures and tables,  
618 can be accessed at <https://github.com/PaddlePaddle/PaddleSeg>.

## 619 9. Conclusion

620 Landslide mapping across extensive geographic areas using remote sensing proves to be  
621 a significant challenge. Although previous attempts have produced landslide datasets and  
622 advanced automation and intelligence, they have not been able to overcome limitations of  
623 specific events and data sources. In this research, we proposed the Globally Distributed  
624 Coseismic Landslide Dataset (GDCLD), an innovative resource crafted to autonomously and  
625 precisely tackle the intricacies of landslide mapping. We made two significant contributions in  
626 this work. Firstly, we meticulously interpreted multi-source remote sensing data to create a  
627 comprehensive dataset for landslide detection. This dataset contains  $1.39 \times 10^9$  annotated  
628 landslide pixels and remote sensing image at four different resolutions, spanning nine global  
629 regions. It successfully addresses the crucial lack of large-scale datasets in current landslide  
630 identification research. Secondly, we utilized GDCLD-trained model to showcase its robustness  
631 and generalization in landslide identification across diverse geographical contexts. Our  
632 proposed dataset shows a great potential in rapid response and emergency management of  
633 geological hazards. Although the landslide samples are obtained from seismic events, the  
634 trained model enable to capture and learn the characteristic differences between landslides  
635 and the surroundings, making them suitable for landslide mapping beyond seismic-triggered  
636 events, such as those caused by rainfall. The comparative analyses with existing datasets  
637 highlight its effectiveness as the data base of deep learning model in mapping landslides across  
638 various global regions. This work has great practical implications for prevention and mitigation  
639 of geological hazard worldwide.



640

## 641 Supplement

642 The supplement related to this article is available online at: XXXX

## 643 Author contributions

644 All the authors contributed equally to the preparation of the paper, from data curation to  
645 the review of the final paper.

646

## 647 Competing Interest

648 The authors declare that they have no known competing financial interests or personal  
649 relationships that could have appeared to influence the work reported in this paper.

650

## 651 Disclaimer.

652 Publisher's note: Copernicus Publications remains neutral with regard to jurisdictional  
653 claims in published maps and institutional affiliations.

654

## 655 Acknowledgements

656 The research is supported by the National Science Fund for Distinguished Young Scholars  
657 of China (Grant No. 42125702), the National Natural Science Foundation of China (Grant No.  
658 42307263), the New Cornerstone Science Foundation through the XPLOER PRIZE (Grant  
659 No. XPLOER-2022-1012), the Natural Science Foundation of Sichuan Province (Grant No.  
660 2022NSFSC0003 and 2022NSFSC1083), and the China Scholarship Council (CSC NO.



661 202409230002). We would like to thank the State Key Laboratory of Geohazard Prevention  
662 and Geoenvironment Protection for providing UAV data, the National Platform for Common  
663 GeoSpatial Information Services for MAP WORLD data, and the China Centre for Resources  
664 Satellite Data and Application for Gaofen-6 data. Thank Kushanav Bhuyan for his assistance  
665 with the language of this paper.

## 666 Reference

- 667 Alpert, L.: Rainfall maps of Hispaniola, *Bulletin of the American Meteorological*  
668 *Society*, 423-431, 1942.
- 669 Basofi, A., Fariza, A., and Dzulkarnain, M. R.: Landslides susceptibility mapping  
670 using fuzzy logic: A case study in Ponorogo, East Java, Indonesia, 2016  
671 International Conference on Data and Software Engineering (ICoDSE), 1-7.
- 672 Bhuyan, K., Tanyaş, H., Nava, L., Puliero, S., Meena, S. R., Floris, M., Van  
673 Westen, C., and Catani, F.: Generating multi-temporal landslide inventories  
674 through a general deep transfer learning strategy using HR EO data,  
675 *Scientific reports*, 13, 162, 2023.
- 676 Brardinoni, F., Slaymaker, O., and Hassan, M. A.: Landslide inventory in a  
677 rugged forested watershed: a comparison between air-photo and field survey  
678 data, *Geomorphology*, 54, 179-196, 2003.
- 679 Burrows, K., Walters, R. J., Milledge, D., Spaans, K., and Densmore, A. L.: A  
680 new method for large-scale landslide classification from satellite radar,  
681 *Remote Sensing*, 11, 237, 2019.
- 682 Calais, E., Symithe, S., Monfret, T., Delouis, B., Lomax, A., Courboux, F.,  
683 Ampuero, J. P., Lara, P. E., Bletery, Q., Cheze, J., Peix, F., Deschamps, A.,  
684 de Lepinay, B., Raimbault, B., Jolivet, R., Paul, S., St Fleur, S., Boisson, D.,  
685 Fukushima, Y., Duputel, Z., Xu, L., and Meng, L.: Citizen seismology helps  
686 decipher the 2021 Haiti earthquake, *Science*, 376, 283-287,  
687 10.1126/science.abn1045, 2022.
- 688 Cao, H., Wang, Y., Chen, J., Jiang, D., Zhang, X., Tian, Q., and Wang, M.: Swin-  
689 unet: Unet-like pure transformer for medical image segmentation, *European*  
690 *conference on computer vision*, 205-218,
- 691 Casagli, N., Intrieri, E., Tofani, V., Gigli, G., and Raspini, F.: Landslide detection,  
692 monitoring and prediction with remote-sensing techniques, *Nature Reviews*  
693 *Earth & Environment*, 4, 51-64, 2023.
- 694 Chau, K. T., Sze, Y., Fung, M., Wong, W., Fong, E., and Chan, L.: Landslide  
695 hazard analysis for Hong Kong using landslide inventory and GIS, *Computers*  
696 *& Geosciences*, 30, 429-443, 2004.
- 697 Chen, B., Xu, B., Zhu, Z., Yuan, C., Suen, H. P., Guo, J., Xu, N., Li, W., Zhao,



- 698 Y., and Yang, J.: Stable classification with limited sample: Transferring a 30-  
699 m resolution sample set collected in 2015 to mapping 10-m resolution global  
700 land cover in 2017, *Sci. Bull.*, 64, 3, 2019.
- 701 Chicco, D. and Jurman, G.: The advantages of the Matthews correlation  
702 coefficient (MCC) over F1 score and accuracy in binary classification  
703 evaluation, *BMC Genomics*, 21, 6, 10.1186/s12864-019-6413-7, 2020.
- 704 Cigna, F., Tapete, D., and Lee, K.: Geological hazards in the UNESCO World  
705 Heritage sites of the UK: From the global to the local scale perspective, *Earth-  
706 Science Reviews*, 176, 166-194, 2018.
- 707 Cigna, F., Osmanoğlu, B., Cabral-Cano, E., Dixon, T. H., Ávila-Olivera, J. A.,  
708 Garduño-Monroy, V. H., DeMets, C., and Wdowinski, S.: Monitoring land  
709 subsidence and its induced geological hazard with Synthetic Aperture Radar  
710 Interferometry: A case study in Morelia, Mexico, *Remote Sensing of  
711 Environment*, 117, 146-161, 2012.
- 712 Coe, J. A., Ellis, W. L., Godt, J. W., Savage, W. Z., Savage, J. E., Michael, J.,  
713 Kibler, J. D., Powers, P. S., Lidke, D. J., and Debray, S.: Seasonal movement  
714 of the Slumgullion landslide determined from Global Positioning System  
715 surveys and field instrumentation, July 1998–March 2002, *Engineering  
716 geology*, 68, 67-101, 2003.
- 717 Dai, L., Fan, X., Wang, X., Fang, C., Zou, C., Tang, X., Wei, Z., Xia, M., Wang,  
718 D., and Xu, Q.: Coseismic landslides triggered by the 2022 Luding Ms6. 8  
719 earthquake, China, *Landslides*, 20, 1277-1292, 2023.
- 720 De Boer, P.-T., Kroese, D. P., Mannor, S., and Rubinstein, R. Y.: A tutorial on the  
721 cross-entropy method, *Annals of operations research*, 134, 19-67, 2005.
- 722 Diakogiannis, F. I., Waldner, F., Caccetta, P., and Wu, C.: ResUNet-a: A deep  
723 learning framework for semantic segmentation of remotely sensed data,  
724 *ISPRS Journal of Photogrammetry and Remote Sensing*, 162, 94-114, 2020.
- 725 Fan, X., Scaringi, G., Xu, Q., Zhan, W., Dai, L., Li, Y., Pei, X., Yang, Q., and  
726 Huang, R.: Coseismic landslides triggered by the 8th August 2017 M s 7.0  
727 Jiuzhaigou earthquake (Sichuan, China): factors controlling their spatial  
728 distribution and implications for the seismogenic blind fault identification,  
729 *Landslides*, 15, 967-983, 2018.
- 730 Fang, C., Fan, X., & Wang, X. (2024). GDCLD [Data set]. Zenodo.  
731 <https://doi.org/10.5281/zenodo.11369484>.
- 732 Fang, C., Fan, X., Zhong, H., Lombardo, L., Tanyas, H., and Wang, X.: A Novel  
733 historical landslide detection approach based on LiDAR and lightweight  
734 attention U-Net, *Remote Sensing*, 14, 4357, 2022.
- 735 Fiorucci, F., Ardizzone, F., Mondini, A. C., Viero, A., and Guzzetti, F.: Visual  
736 interpretation of stereoscopic NDVI satellite images to map rainfall-induced  
737 landslides, *Landslides*, 16, 165-174, 2019.
- 738 Fiorucci, F., Cardinali, M., Carlà, R., Rossi, M., Mondini, A., Santurri, L.,  
739 Ardizzone, F., and Guzzetti, F.: Seasonal landslide mapping and estimation



- 740 of landslide mobilization rates using aerial and satellite images,  
741 *Geomorphology*, 129, 59-70, 2011.
- 742 Gao, H., Yin, Y., Li, B., Gao, Y., Zhang, T., Liu, X., and Wan, J.: Geomorphic  
743 evolution of the Sedongpu Basin after catastrophic ice and rock avalanches  
744 triggered by the 2017 Ms6. 9 Milin earthquake in the Yarlung Zangbo River  
745 area, China, *Landslides*, 1-15, 2023.
- 746 Gao, J. and Maro, J.: Topographic controls on evolution of shallow landslides  
747 in pastoral Wairarapa, New Zealand, 1979–2003, *Geomorphology*, 114, 373-  
748 381, 2010.
- 749 Ghorbanzadeh, O., Xu, Y., Zhao, H., Wang, J., Zhong, Y., Zhao, D., Zang, Q.,  
750 Wang, S., Zhang, F., and Shi, Y.: The outcome of the 2022 landslide4sense  
751 competition: Advanced landslide detection from multisource satellite imagery,  
752 *IEEE Journal of Selected Topics in Applied Earth Observations and Remote*  
753 *Sensing*, 15, 9927-9942, 2022.
- 754 Gorum, T., Fan, X., van Westen, C. J., Huang, R. Q., Xu, Q., Tang, C., and  
755 Wang, G.: Distribution pattern of earthquake-induced landslides triggered by  
756 the 12 May 2008 Wenchuan earthquake, *Geomorphology*, 133, 152-167,  
757 2011.
- 758 Guzzetti, F., Mondini, A. C., Cardinali, M., Fiorucci, F., Santangelo, M., and  
759 Chang, K.-T.: Landslide inventory maps: New tools for an old problem, *Earth-*  
760 *Science Reviews*, 112, 42-66, 2012.
- 761 Harp, E. L., Jibson, R. W., and Schmitt, R. G.: Map of landslides triggered by  
762 the January 12, 2010, Haiti earthquake, US Geological Survey Scientific  
763 Investigations Map, 3353, 15, 2016.
- 764 He, K., Zhang, X., Ren, S., and Sun, J.: Deep residual learning for image  
765 recognition, *Proceedings of the IEEE conference on computer vision and*  
766 *pattern recognition*, 770-778,
- 767 Hu, K., Zhang, X., You, Y., Hu, X., Liu, W., and Li, Y.: Landslides and dammed  
768 lakes triggered by the 2017 Ms6. 9 Milin earthquake in the Tsangpo gorge,  
769 *Landslides*, 16, 993-1001, 2019.
- 770 Huang, R. and Fan, X.: The landslide story, *Nature Geoscience*, 6, 325-326,  
771 2013.
- 772 Huang, R., Pei, X., Fan, X., Zhang, W., Li, S., and Li, B.: The characteristics  
773 and failure mechanism of the largest landslide triggered by the Wenchuan  
774 earthquake, May 12, 2008, China, *Landslides*, 9, 131-142, 2012.
- 775 Huang, Y., Xu, C., Zhang, X., Xue, C., and Wang, S.: An Updated Database and  
776 Spatial Distribution of Landslides Triggered by the Milin, Tibet M w6. 4  
777 Earthquake of 18 November 2017, *Journal of Earth Science*, 32, 1069-1078,  
778 2021.
- 779 Ji, S., Yu, D., Shen, C., Li, W., and Xu, Q.: Landslide detection from an open  
780 satellite imagery and digital elevation model dataset using attention boosted  
781 convolutional neural networks, *Landslides*, 17, 1337-1352, 2020.



- 782 Li, Z., Shi, W., Lu, P., Yan, L., Wang, Q., and Miao, Z.: Landslide mapping from  
783 aerial photographs using change detection-based Markov random field,  
784 Remote sensing of environment, 187, 76-90, 2016.
- 785 Liu, J., Huang, X., Song, G., Li, H., and Liu, Y.: Uninet: Unified architecture  
786 search with convolution, transformer, and mlp, European Conference on  
787 Computer Vision, 33-49,
- 788 Liu, Z., Lin, Y., Cao, Y., Hu, H., Wei, Y., Zhang, Z., Lin, S., and Guo, B.: Swin  
789 transformer: Hierarchical vision transformer using shifted windows,  
790 Proceedings of the IEEE/CVF international conference on computer vision,  
791 10012-10022,
- 792 Loshchilov, I. and Hutter, F.: Decoupled weight decay regularization, arXiv  
793 preprint arXiv:1711.05101, 2017.
- 794 Lu, P., Qin, Y., Li, Z., Mondini, A. C., and Casagli, N.: Landslide mapping from  
795 multi-sensor data through improved change detection-based Markov random  
796 field, Remote Sensing of Environment, 231, 111235, 2019.
- 797 Luppino, L. T., Hansen, M. A., Kampffmeyer, M., Bianchi, F. M., Moser, G.,  
798 Jenssen, R., and Anfinson, S. N.: Code-Aligned Autoencoders for  
799 Unsupervised Change Detection in Multimodal Remote Sensing Images,  
800 IEEE Trans Neural Netw Learn Syst, PP, 10.1109/TNNLS.2022.3172183,  
801 2022.
- 802 Ma, Y., Yu, D., Wu, T., and Wang, H.: PaddlePaddle: An open-source deep  
803 learning platform from industrial practice, Frontiers of Data and Computing,  
804 1, 105-115, 2019.
- 805 Meena, S. R., Ghorbanzadeh, O., van Westen, C. J., Nachappa, T. G., Blaschke,  
806 T., Singh, R. P., and Sarkar, R.: Rapid mapping of landslides in the Western  
807 Ghats (India) triggered by 2018 extreme monsoon rainfall using a deep  
808 learning approach, Landslides, 18, 1937-1950, 2021.
- 809 Meena, S. R., Nava, L., Bhuyan, K., Puliero, S., Soares, L. P., Dias, H. C., Floris,  
810 M., and Catani, F.: HR-GLDD: A globally distributed dataset using  
811 generalized DL for rapid landslide mapping on HR satellite imagery, Earth  
812 System Science Data Discussions, 1-21, 2022.
- 813 Metternicht, G., Hurni, L., and Gogu, R.: Remote sensing of landslides: An  
814 analysis of the potential contribution to geo-spatial systems for hazard  
815 assessment in mountainous environments, Remote sensing of Environment,  
816 98, 284-303, 2005.
- 817 Mondini, A. C., Guzzetti, F., Chang, K.-T., Monserrat, O., Martha, T. R., and  
818 Manconi, A.: Landslide failures detection and mapping using Synthetic  
819 Aperture Radar: Past, present and future, Earth-Science Reviews, 216,  
820 103574, 2021.
- 821 Nava, L., Monserrat, O., and Catani, F.: Improving landslide detection on SAR  
822 data through deep learning, IEEE Geoscience and Remote Sensing Letters,  
823 19, 1-5, 2021.





- 824 O'Shea, K. and Nash, R.: An introduction to convolutional neural networks,  
825 arXiv preprint arXiv:1511.08458, 2015.
- 826 Poveda, E., Pedraza, P., Velandia, F., Mayorga, E., Plicka, V., Gallovič, F., and  
827 Zahradník, J.: 2019 Mw 6.0 Mesetas (Colombia) Earthquake Sequence:  
828 Insights From Integrating Seismic and Morphostructural Observations, *Earth  
829 and Space Science*, 9, e2022EA002465, 2022.
- 830 Rezatofghi, H., Tsoi, N., Gwak, J., Sadeghian, A., Reid, I., and Savarese, S.:  
831 Generalized intersection over union: A metric and a loss for bounding box  
832 regression, *Proceedings of the IEEE/CVF conference on computer vision  
833 and pattern recognition*, 658-666,
- 834 Ronneberger, O., Fischer, P., and Brox, T.: U-net: Convolutional networks for  
835 biomedical image segmentation, *Medical Image Computing and Computer-  
836 Assisted Intervention–MICCAI 2015: 18th International Conference, Munich,  
837 Germany, October 5-9, 2015, Proceedings, Part III* 18, 234-241,
- 838 Shao, X., Ma, S., and Xu, C.: Distribution and characteristics of shallow  
839 landslides triggered by the 2018 Mw 7.5 Palu earthquake, Indonesia,  
840 *Landslides*, 20, 157-175, 2023.
- 841 Soares, L. P., Dias, H. C., Garcia, G. P. B., and Grohmann, C. H.: Landslide  
842 segmentation with deep learning: Evaluating model generalization in rainfall-  
843 induced landslides in Brazil, *Remote Sensing*, 14, 2237, 2022.
- 844 Tang, D., Ge, W., and Cao, X.: Stress triggering of the 2022 Lushan–Maerkang  
845 earthquake sequence by historical events and its implication for fault stress  
846 evolution in eastern Tibet, *Frontiers in Earth Science*, 11, 1105394, 2023.
- 847 Townsend, J. T.: Theoretical analysis of an alphabetic confusion matrix,  
848 *Perception & Psychophysics*, 9, 40-50, 1971.
- 849 Udin, W., Norazami, N., Sulaiman, N., Zaudin, N. C., Ma'ail, S., and Nor, A. M.:  
850 UAV based multi-spectral imaging system for mapping landslide risk area  
851 along Jeli-Gerik highway, Jeli, Kelantan, 2019 *IEEE 15th International  
852 Colloquium on Signal Processing & Its Applications (CSPA)*, 162-167,
- 853 Valagussa, A., Marc, O., Frattini, P., and Crosta, G. B.: Seismic and geological  
854 controls on earthquake-induced landslide size, *Earth and Planetary Science  
855 Letters*, 506, 268-281, 2019.
- 856 Wang, F., Fan, X., Yunus, A. P., Siva Subramanian, S., Alonso-Rodriguez, A.,  
857 Dai, L., Xu, Q., and Huang, R.: Coseismic landslides triggered by the 2018  
858 Hokkaido, Japan (M w 6.6), earthquake: spatial distribution, controlling  
859 factors, and possible failure mechanism, *Landslides*, 16, 1551-1566, 2019.
- 860 Wang, J., Sun, K., Cheng, T., Jiang, B., Deng, C., Zhao, Y., Liu, D., Mu, Y., Tan,  
861 M., and Wang, X.: Deep high-resolution representation learning for visual  
862 recognition, *IEEE transactions on pattern analysis and machine intelligence*,  
863 43, 3349-3364, 2020.
- 864 Xiao, T., Liu, Y., Zhou, B., Jiang, Y., and Sun, J.: Unified perceptual parsing for  
865 scene understanding, *Proceedings of the European conference on computer*



- 866 vision (ECCV), 418-434,  
867 Xie, E., Wang, W., Yu, Z., Anandkumar, A., Alvarez, J. M., and Luo, P.:  
868 SegFormer: Simple and efficient design for semantic segmentation with  
869 transformers, *Advances in Neural Information Processing Systems*, 34,  
870 12077-12090, 2021.
- 871 Xu, Y., Ouyang, C., Xu, Q., Wang, D., Zhao, B., and Luo, Y.: CAS Landslide  
872 Dataset: A Large-Scale and Multisensor Dataset for Deep Learning-Based  
873 Landslide Detection, *Sci Data*, 11, 12, 10.1038/s41597-023-02847-z, 2024.
- 874 Yamagishi, H. and Yamazaki, F.: Landslides by the 2018 hokkaido iburi-tobu  
875 earthquake on september 6, *Landslides*, 15, 2521-2524, 2018.
- 876 Yang, Z., Xu, C., and Li, L.: Landslide detection based on ResU-net with  
877 transformer and CBAM embedded: two examples with geologically different  
878 environments, *Remote Sensing*, 14, 2885, 2022a.
- 879 Yang, Z., Dai, D., Zhang, Y., Zhang, X., and Liu, J.: Rupture process and  
880 aftershock mechanisms of the 2022 Luding M6. 8 earthquake in Sichuan,  
881 China, *Earthquake Science*, 35, 1-2, 2022b.
- 882 Ye, C., Li, Y., Cui, P., Liang, L., Pirasteh, S., Marcato, J., Goncalves, W. N., and  
883 Li, J.: Landslide detection of hyperspectral remote sensing data based on  
884 deep learning with constrains, *IEEE Journal of Selected Topics in Applied  
885 Earth Observations and Remote Sensing*, 12, 5047-5060, 2019.
- 886 Yi, Y., Zhang, Z., Zhang, W., Jia, H., and Zhang, J.: Landslide susceptibility  
887 mapping using multiscale sampling strategy and convolutional neural  
888 network: A case study in Jiuzhaigou region, *Catena*, 195, 104851, 2020.
- 889 Zhang, X., Yu, W., Pun, M.-O., and Shi, W.: Cross-domain landslide mapping  
890 from large-scale remote sensing images using prototype-guided domain-  
891 aware progressive representation learning, *ISPRS Journal of  
892 Photogrammetry and Remote Sensing*, 197, 1-17, 2023.
- 893 Zhao, B., Li, W., Su, L., Wang, Y., and Wu, H.: Insights into the landslides  
894 triggered by the 2022 Lushan Ms 6.1 earthquake: spatial distribution and  
895 controls, *Remote Sensing*, 14, 4365, 2022a.
- 896 Zhao, B., Wang, Y., Li, W., Lu, H., and Li, Z.: Evaluation of factors controlling  
897 the spatial and size distributions of landslides, 2021 Nippes earthquake, Haiti,  
898 *Geomorphology*, 415, 108419, 2022b.
- 899 Zhong, C., Liu, Y., Gao, P., Chen, W., Li, H., Hou, Y., Nuremanguli, T., and Ma,  
900 H.: Landslide mapping with remote sensing: challenges and opportunities,  
901 *International Journal of Remote Sensing*, 41, 1555-1581, 2020.
- 902